Water Reuse

IWA PUBLISHING

Water Reuse Vol 12 No 1, 111 doi: 10.2166/wrd.2022.103

Adsorption of phosphorus onto nanoscale zero-valent iron/activated carbon: removal mechanisms, thermodynamics, and interferences

Adel Adly[a], Nagwan G. Mostafa[b] and Abdelsalam Elawwad[b,*]

[a] Canadian International College, Faculty of Engineering, Giza 16242, Egypt
[b] Public Works Department, Cairo University, Faculty of Engineering, Giza 12613, Egypt
*Corresponding author. E-mail: elawwad@cu.edu.eg

AE, 0000-0002-9202-870X

ABSTRACT

This study investigated removal mechanisms, thermodynamics, and interferences of phosphorus adsorption onto nanoscale zero-valent iron (nZVI)/activated carbon composite. Activated carbon was successfully used as support for nZVI particles to overcome shortcomings of using nZVI include its tendency to aggregate and separation difficulties. A comprehensive characterization was done for the composite particles, which revealed a high specific surface area of 72.66 m^2/g and an average particle size of 37 nm. Several adsorption isotherms and kinetic models have been applied to understand the removal mechanisms. Adsorption isotherm is best fitted by Freundlich and Langmuir models, which indicates that the estimated maximum phosphorus adsorption capacity is 53.76 mg/g at pH 4. Adsorption kinetics showed that the chemisorption process behaved according to a pseudo-second-order model. An adsorption mechanism study conducted using the intra-particle diffusion and Boyd kinetic models indicated that the adsorption rate is limited by surface diffusion. A thermodynamic study showed that phosphorus removal efficiency increased as the solution temperature increased from 15 to 37 °C. Finally, the results of an interference study showed that the presence of Ni^{2+}, Cu^{2+}, Ca^{2+}, Na^{+} cations, nitrate ions (NO_3^-), and sodium acetate improves removal efficiency, while the presence of sulfate ions (SO_4^{2-}) and urea reduces removal efficiency.

Key words: activated carbon, adsorption, isotherm, nanoscale zero-valent iron, phosphorus

HIGHLIGHTS

- Successful synthesis of nZVI/AC composite with a specific surface area of 72.66 m^2/g.
- Characterization of the composite using SEM, EDX, XRD, BET SSA, FTIR, and TAG.
- Langmuir adsorption isotherm model is best fitted phosphorus adsorption on nZVI/AC.
- nZVI/AC composite had a superior phosphorus adsorption capacity was 53.76 mg/g.
- Phosphorus adsorption rate was controlled by surface diffusion.

GRAPHICAL ABSTRACT

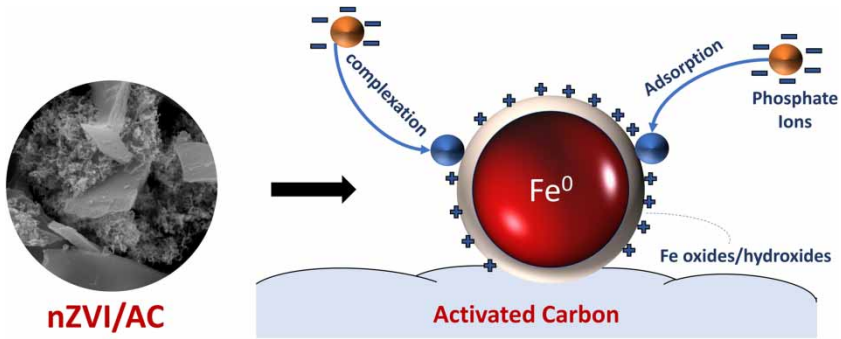

1. INTRODUCTION

Phosphorus is a substantial macronutrient for the growth of all forms of life in aquatic environments. However, it is also considered to be a limiting element of the eutrophication process in water bodies (Maamoun *et al.* 2021). The eutrophication process occurs when a water body becomes progressively enriched with minerals and nutrients such that it encourages the excessive growth of plants and algae (Tu & You 2014). Eutrophication results in lower levels of light transmission and the depletion of dissolved oxygen in water, which leads to the death of fish and negatively affects other forms of aquatic life by decreasing biodiversity (He *et al.* 2018).

The phosphorus concentration of the effluent wastewater from WWTPs, desalination plants, and textile industries needs to be treated before discharging it into water bodies (Panagopoulos 2021). Phosphorus removal from wastewater is usually carried out by biological treatment or chemical precipitation (Trinh *et al.* 2020). The advantages of biological treatment are that there is no need to use chemicals and produce less sludge (Elawwad & Hazem 2017). However, this process tends to be sensitive to variations in the characteristics of the wastewater, such as the existence of toxic pollutants and temperature; this makes its application inconvenient, especially in the case of industrial wastewater, and often fails to achieve the permissible regulatory limits before it can be discharged into the environment (Elawwad *et al.* 2016). In contrast, chemical precipitation processes are extensively used to remove phosphorus, especially from industrial wastewater, because of its effectiveness and ease of operation. However, chemical precipitation requires costly metal salts, produces high quantities of sludge, and increases dissolved solids in the treated water (Wu *et al.* 2013a). The chemicals used in phosphorus removal are primarily aluminum and iron salts. Thus, the chemical precipitation of phosphorus with metal cations is an efficient method for the removal of phosphorus from wastewater, but is inconvenient for wastewater with high phosphorus content because of the consumption of large amounts of chemicals and the increase of ions in the treated water, which can be considered to be a form of secondary pollution (Wen *et al.* 2014). Hence, more innovative techniques are required to address the drawbacks of the aforementioned approaches to phosphorus removal. Adsorption appears to be one of the most promising technologies for phosphorus removal as it is simple to operate, has a high removal efficiency, and is cost-effective. Recently, the removal of phosphorus from aqueous solutions by adsorption has attracted much attention (Li *et al.* 2019).

Several different low-cost adsorbents such as fly ash, active red mud, steel slag, iron humate, and zirconium were examined for their ability to remove phosphorus from aqueous solutions (Trinh *et al.* 2020). However, the primary disadvantage for these adsorbents has been their low phosphorus adsorption capacity, which has restricted their practical applications. Furthermore, specific adsorbents such as natural minerals comprised of organic pollutants and heavy metals could be released into the water during the treatment process, causing secondary pollution (Wen *et al.* 2014). The economic concerns and adsorption capacity are not only the aspects that define the most appropriate sorbent – the ability of sorbent to adapt to diverse pH values and other constituents present in wastewater must also be considered (Wu *et al.* 2013a).

In recent years, nZVI particles have been widely studied for the treatment of various contaminants, such as nitroaromatic compounds, chlorinated organic contaminants, heavy metal ions, phosphate, and nitrates (Li *et al.* 2021; Tarekegn *et al.* 2021). Although nZVI has exhibited superior performances in many applications due to its high surface reactivity and large surface areas, it has several shortcomings; nZVI particles are fine powders that have a strong tendency to aggregate into larger particles, forming necklace-like structures due to their high surface energy and active magnetic interaction (Khalil *et al.* 2017). Moreover, the separation of individual nZVI particles is very difficult. Therefore, the direct application of nZVI for remediation in water treatment processes may expose both the aquatic ecosystems and human health to definite risks because of nZVI potential pollution of drinking water by iron (Gosu *et al.* 2016). These shortcomings can be overcome by supporting nZVI with solid porous materials, such as silica, resin, clays, zeolite, polymer membranes, and activated carbon (AC) (Qian *et al.* 2017). These materials are effective at decreasing the clumping and aggregation of nZVI by dispersing its particles on the porous surface of the material, consequently improving reactivity and the ease of separation of the nZVI particles (Qian *et al.* 2017). The immobilization of nZVI particles by a porous support material can be carried out by fixing nZVI onto the surface of the support material or by trapping nZVI inside its pores (Stefaniuk *et al.* 2016).

In previous studies, nZVI particles have shown several removal mechanisms for different contaminants. These removal mechanics include physical or chemical adsorption, ion exchange, co-precipitation, and rate-controlled diffusion (Maamoun *et al.* 2021). Few studies focused on understanding the adsorption mechanisms of phosphorus onto nZVI (Maamoun *et al.* 2021). Hence, there is a need to realize the main mechanisms that are involved in each removal process for phosphorus removal. Although nZVI particles were used on a wide scale for heavy metals and organic contaminants removal (Almeelbi

& Bezbaruah 2014; Wen *et al.* 2014; Renu *et al.* 2017), few research papers discuss supported nZVI for phosphorus removal. Liu *et al.* (2014) and Soliemanzadeh & Fekri (2017) studied the removal of phosphorus using graphene-supported nZVI and clay-supported nZVI, respectively. Zhou *et al.* (2014) investigated the potential biochar-supported zero-valent iron for the removal of various contaminants, including phosphorus; however, the study did not include kinetics or isotherm studies. Ma *et al.* (2020) studied the removal mechanism of phosphorus onto rape straw biochar-supported nZVI; however, it showed a maximum adsorption capacity of 12.14 mg/g which is low compared to the literature.

Despite the aforementioned studies, limited studies investigated the removal mechanism for phosphorus adsorption onto nanoscale zero-valent iron/activated carbon, and to our knowledge, no study investigated the thermodynamics and interferences for this particular case. Thus, the objectives of this study were (1) to study the influence of some factors, namely initial solution pH, adsorbent dosage, rotation speed of the shaker, initial phosphorus concentration, and temperature, on phosphorus removal efficiency; (2) to study the adsorption isotherm and kinetics under the achieved best conditions, to recognize the phosphorus removal mechanics using nZVI/AC; (3) to conduct thermodynamic analysis in order to evaluate the thermal characteristics of phosphorus removal using nZVI/AC; and (4) to conduct an interference study to investigate the influence of the presence of interfering ions and organic compounds on the efficacy of phosphorus removal in order to simulate realistic conditions for the application of nZVI/AC in wastewater, allowing for the identification of more effective and environmentally friendly methods of removing phosphorus from wastewaters, especially in solutions with high phosphorus concentrations.

nZVI/AC composite was successfully synthesized borohydride reduction method and characterized using Scanning Electron Microscopy (SEM), Energy-dispersive X-ray (EDX), Brunauer–Emmett–Teller (BET), Fourier transform infrared spectroscopy (FTIR), X-ray diffraction (XRD), and Thermo-gravimetric analysis (TGA) were used to characterize the prepared composite to study its microstructure, specific surface area (SSA), porous surface details, and physical and chemical properties.

2. MATERIALS AND METHODS

2.1. Preparation of nZVI/AC particles

nZVI/AC particles were synthesized following the methods described by previous studies (Gosu *et al.* 2016; Khalil *et al.* 2017; Qian *et al.* 2017) and the preparation steps are summarized in Figure 1. Initially, 1.0 g of ferric chloride ($FeCl_3{\cdot}6H_2O$, 99.0%, Loba Chemie, India) and 0.5 g of activated carbon (Charcoal Activated 'Steam activation', Advent Chembio., India) with a ratio 2:1 of nZVI:AC was determined to be the optimal ratio (Khalil *et al.* 2017) and they were combined in 50 mL of distilled water. Subsequently, the pH of the solution was adjusted to 4.0, then agitated with a rotary shaker at a speed of 150 rpm and a temperature of 25 °C for 2 h. Following this, the solution was conveyed to a three-neck flask in addition to 50 mL of ethanol. The produced mixture was purged by introducing a nitrogen gas stream into the solution for 1 h to remove any dissolved oxygen; this step was conducted while the solution was being strongly stirring. 100 mL of 0.5 M sodium borohydride ($NaBH_4$, 98.0%, Research Lab Fine Chem Industries, India) solution was poured into a burette and added to the slurry under rapid stirring (drop by drop, 1 drop per 2 seconds). After the addition of sodium borohydride, the solution was mixed for an additional 30 min until no significant production of H_2 was observed (Fu *et al.* 2013). The following equation describes the reduction of ferric iron to zero-valent iron (Fe^0) (Wen *et al.* 2014):

$$4\,Fe^{3+} + 3\,BH_4^- + 9\,H_2O \rightarrow 4\,Fe^0\downarrow + 3\,H_2BO^{3-} + 12\,H^+ + 6\,H_2\uparrow \quad (1)$$

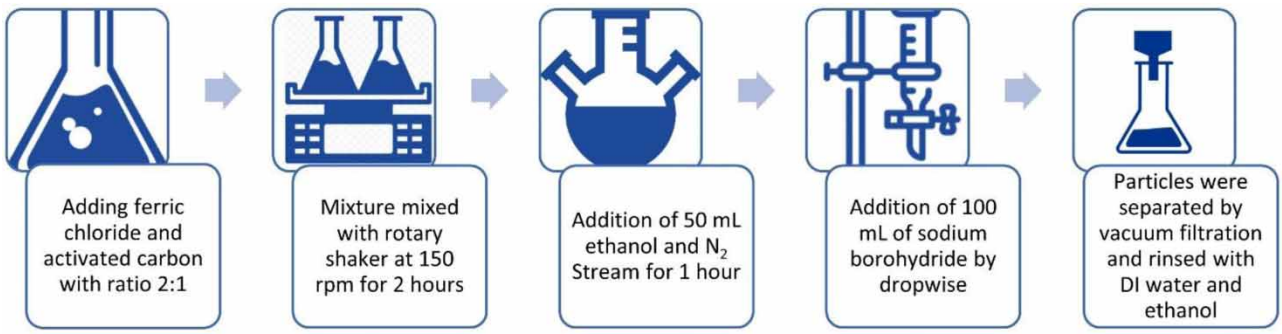

Figure 1 | Illustration diagram of preparation steps of nZVI/AC particles.

The next step in the synthesis of nZVI/AC is the washing step, which is considered to be a key process since it prevents the rapid oxidation of the zero-valent iron nanoparticles. After the reaction was complete, the samples of nZVI/AC were separated from the solution by using vacuum filtration and two sheets of Whatman's (Qualitative 2) filter papers. Subsequently, the solids were rinsed with deionized (DI) water several times, followed by an additional three washes with 25 mL of absolute ethanol (C_2H_5OH, 99.5%, El Nasr Pharmaceutical Chemical Company, Egypt) to remove any remaining water. Finally, the solids were vacuum dried at 60 °C overnight and stored in an N_2-purged desiccator to prevent the oxidation of the nanoscale iron particles.

An SEM (Quanta, Model 250 FEG, USA) was used to understand the surface morphology of the synthesized nZVI/AC. A sample of the synthesized nZVI/AC was initially gold coated with a sputter coater for 30 s, which increases the conductivity of the sample; following this, SEM images were taken. The EDX analysis was conducted in conjunction with the SEM analysis to determine the chemical composition of the nZVI/AC sample. The crystallinity and composition of the synthesized nZVI/AC were investigated using XRD (Empyrean X-ray diffraction, Malvern Panalytical, UK). The samples were put on stainless steel sample holders and analyzed using Cu K_α radiation ($\lambda = 1.54$ Å) operated at 45 kV and 30 mA. The scanning step size was 0.026° between 3° and 90°.

The BET SSA and porosity of the sample were determined using nitrogen gas adsorption at 77 K via a surface characterization analyzer (Quantachrome TouchWin v1.2). The samples were dried, placed in tubes, and degassed under a nitrogen gas stream at 350 °C for 2 h prior to the measurement. FTIR was used to indicate the presence of functional groups and complexes in the nZVI/AC sample before and after treatment, and was carried out at room temperature using an FTIR-4100 type (A) spectrometer (JASCO., USA). The samples were prepared by mixing 1 mg of nZVI/AC particles with 100 mg of Potassium Bromate (KBr) powder. A thermo-gravimetric analyzer TGA-50/50H (Shimadzu, Japan) was used to analyze the nZVI/AC sample. The initial weight of the sample was 5.311 mg. The temperature was raised from 50 to 800 °C with a heating rate of 10 °C/min for 75 min. The combustion process was carried out in the presence of nitrogen gas. The weight of the sample was recorded every second during the analysis.

2.2. Phosphate batch experiments

A stock solution of 100 mg/L phosphorus concentration was prepared by dissolving potassium dihydrogen phosphate (KH_2PO_4, 99.5%, Loba Chemie, India) in DI water. The required concentrations were prepared by diluting the stock solution (Soliemanzadeh & Fekri 2017).

The pH values of the batch solutions were adjusted by adding droplets of prepared 0.1 M HCL or 0.1 M NaOH solutions. During the batch experiments, five 5 mL samples were drawn at pre-defined time intervals of 5, 15, 30, 60, and 90 min. The samples were subsequently filtered using Whatman No. 43 filter paper and were analyzed to determine the decrease in the phosphorus concentration using a DR/4000 U Spectrophotometer, 115 Vac.

An initial batch experiment was carried out under both aerobic and anaerobic conditions to identify the conditions that were more suitable for phosphorus removal. Aerobic conditions were achieved by leaving the flask open to the air, while anaerobic conditions were attained by deoxygenating the solution through the injection of nitrogen gas for 30 min before the start of the experiment as suggested by Eljamal *et al.* (2016).

Five aerobic batch experiments were carried out to examine the following parameters; pH, adsorbent dose, shaker rotation speed, initial phosphorus concentration, and temperature in order to identify the ideal operating conditions. The batch experiments were conducted such that once a parameter was tested and its optimal value obtained, this value would be held constant during the following batches as summarized in Table 1. Batch experiments were carried out in the following order: (1) batches that varied the pH value of the initial solution were conducted at values of 3, 4, 5, 6, 7, and 9; (2) nZVI/AC dose batches were conducted at values of 0.25, 0.5, 1, 1.5, and 2 g/L, (3) orbital shaker rotation speeds were examined at values of 100, 150, 200, and 250 rpm, (4) initial phosphorus concentration (C_0) in the solution batches were conducted at values of 20, 30, 40, and 50 mg P/L, and finally (5) ambient air temperature (T) batches were conducted at values of 15, 26, and 37 °C.

In addition, a batch experiment containing only activated carbon (AC) was conducted to examine the removal performance of AC without nZVI; this was performed with a dose of 100 mg activated carbon powder in 100 mL phosphorus solution with a concentration of 50 mg/L PO_4^{-3}.

The first batch of experiments varied the pH of the initial solution. The pH of the solution was measured by a pH meter whenever the shaker was stopped. The pH values of each solution were collected throughout the experiment and analyzed to study the effect of the adsorption process on the solution pH. Studying the changes in pH value during the adsorption process

Table 1 | Parameters examined in the batch experiments

Batch	Selected parameters from previous batch	Tested parameter	Test values	Optimum value
1	–	pH	3, 4, 5, 6, 7, and 9	4
2	• pH = 4	nZVI/AC dose	0.25, 0.5, 1.0, 1.5, and 2.0 g/L	1.0 g/L
3	• pH = 4 • nZVI/AC dose = 1.0 g/L	Shaker rotation speed	100, 150, 200, and 250 rpm	200 rpm
4	• pH = 4 • nZVI/AC dose = 1.0 g/L • Shaker rotation speed = 200 rpm	Initial phosphorus concentration (C_0)	20, 30, 40, and 50 mg P/L	50 mg P/L
5	• pH = 4 • nZVI/AC dose = 1.0 g/L • Shaker rotation speed = 200 rpm • Initial phosphorus concentration (C_0) = 50 mg/L	Ambient air temperature (T)	15, 26, and 37 °C	26 °C

was extremely important, as the final pH value of the solution strongly controls the solubility of the nZVI particles in water. If the nZVI particles dissolved in the solution, they could escape the filtration process and cause iron pollution in the resultant solution.

The adsorption kinetics and isotherm experiments were conducted by varying the initial phosphorus concentration. Therefore, the experiments that varied the initial phosphorus concentration (Batch 4) were conducted with an extended period (up to 5 h), such that the equilibrium state of the solutions was reached; this was done because the models that describe adsorption kinetics and isotherms depend on the pollutant reaching an equilibrium concentration in the solution. Samples from Batch 4 were withdrawn at pre-defined time intervals of 5, 15, 30, 60, 90, 120, 180, 240, and 300 min. The phosphorus adsorption capacity, q_t (mg adsorbate/g adsorbent), and phosphorus removal efficiency are determined by the following equations:

$$q_t = \frac{(C_0 - C_t) * V}{m} \tag{2}$$

$$\text{Removal } \% = \frac{(C_0 - C_t)}{C_0} * 100\% \tag{3}$$

where C_0 and C_t are the phosphorus concentrations (mg/L) at times 0 and t, respectively; V is the volume of the solution (mL); and m is the mass of nZVI/AC particles (g).

The adsorption of phosphorus on nZVI/AC particles was analyzed using four isotherms models; Freundlich (Equation (4)), Langmuir (Equation (5)), Temkin (Equation (6)), and Dubinin–Radushkevich (D–R) (Equation (7)). The linear forms of the models are expressed in the following equations:

$$\log q_e = \log K_F + \frac{1}{n} \log C_e \tag{4}$$

$$\frac{C_e}{q_e} = \frac{1}{K_L q_m} + \frac{C_e}{q_m} \tag{5}$$

$$q_e = \frac{RT}{b} \ln K_T + \frac{RT}{b} \ln C_e \tag{6}$$

$$\ln q_e = \ln q_d - \beta * \varepsilon^2 \tag{7}$$

where q_e is the equilibrium adsorption capacity (mg/g); C_e is the equilibrium concentration of phosphorus (mg/L); K_F and $1/n$ are the Freundlich isotherm constants associated with adsorption capacity and intensity, respectively. q_m is the maximum adsorption capacity (mg/g); K_L is the Langmuir isotherm constant related to the adsorption energy (L/mg); b is the Temkin constant related to the heat of sorption (J/mol); K_T was the Temkin isotherm constant (L/g); R is the universal gas constant (8.314 J/mol K); T is the temperature of the solution in kelvin (K); q_d is the D–R constant related to the maximum coverage (mg/g), β is the constant associated to adsorption energy, and ε is the Polanyi potential which is equal to $RT\ln(1+1/c_e)$ (Çelebi *et al.* 2007; Boparai *et al.* 2011; Wen *et al.* 2014).

In this study, three models were applied to describe the sorption kinetics of phosphorus on nZVI/AC particles; pseudo-first-order (Equation (8)), pseudo-second-order (Equation (9)), and the Elovich equation (Equation (10)), as follows:

$$\ln(q_e - q_t) = \ln q_e - K_1 \cdot t \tag{8}$$

$$\frac{t}{q_t} = \frac{t}{q_e} + \frac{1}{K_2 \cdot q_e^2} \tag{9}$$

$$q_t = \frac{1}{\beta}\ln(\alpha\beta) + \frac{1}{\beta}\ln(t) \tag{10}$$

$$h = k_2 q_e^2 \tag{11}$$

where t is the contact time (h); q_e and q_t are adsorption capacities (mg/g) at equilibrium and time t, respectively. k_1 is the pseudo-first-order rate constant (h^{-1}) and k_2 is the pseudo-second-order rate constant (g/mg h). h (mg/g h) is the initial adsorption rate constant calculated using Equation (11). α (mg/g h) and β (g/mg) are the initial adsorption rate constant and the Elovich adsorption constant, respectively, and are related to the extent of surface coverage (Mezenner & Bensmaili 2009; Senthil Kumar *et al.* 2011; Yoon *et al.* 2014).

Thermodynamic experiments were conducted by varying the ambient air temperature. Hence, experiments that varied the ambient air temperature (Batch 5) were conducted over an extended period of up to 7 h. This was done to better understand the effect of temperature on the efficiency of phosphorus removal by nZVI/AC.

2.3. Batch experiments for interference studies

Interference studies were conducted to simulate real-world conditions and applications, as well as to observe the variation in nZVI/AC phosphorus removal efficiency under the influence of various interference substances. The interference batches were carried out under optimal operation conditions as determined from the previous batch experiments. The parameters were adjusted to an initial pH of 4, an nZVI/AC dose of 1 g/L, a shaker rotation speed of 200 rpm, an initial phosphorus concentration of 50 mg P/L, and an ambient temperature of 26 ± 2 °C. The difference in the removal performance between batches was compared over a 3-h period, and the samples were extracted at time intervals of 5, 15, 30, 60, 90, 120, and 180 min.

Firstly, a batch of experiments using a solution containing solely phosphorus was examined in parallel with the batches for the interference study. This batch of experiments was regarded as a control for the interference studies and was used to determine if the interfering substances had enhancing or inhibitory effects on the efficiency of phosphorus removal.

The interference effects of cations (Ni^{2+}, Cu^{2+}, Ca^{2+}, Na^{+}), anions (SO_4^{2-}, NO_3^{-}), the hardness of the solution (determined by the calcium carbonate content of the solution), and the presence of organic matter (urea and sodium acetate) were investigated. The cation batches were conducted with nickel chloride ($NiCl_2$, 200 mg/L), copper sulfate ($CuSO_4$, 100 mg/L), calcium chloride ($CaCl_2$, 500 mg/L) and sodium chloride (NaCl, 500 mg/L). The anion batches were examined by using potassium sulfate (K_2SO_4; 500 mg/L) and potassium nitrate (KNO_3; 100 mg/L). The hardness of the batch solution was adjusted by adding specific amounts of calcium carbonate ($CaCO_3$); a soft and hard solution was prepared using 40 and 180 mg/L $CaCO_3$, respectively. Finally, the effects of the presence of organic matter in wastewater were examined by adding urea (CH_4N_2O) and sodium acetate ($C_2H_3NaO_2$) with concentrations of 100 and 50 mg/L, respectively. These concentrations were chosen to simulate the maximum interference conditions that can be present in real-world wastewater (Almeelbi & Bezbaruah 2014; Khalil *et al.* 2018).

The phosphate concentrations were colorimetrically determined by using a UV–Vis spectrophotometer (DR 4000, Hach Co., USA). Phosphorus was measured using the stannous chloride method at a wavelength of 690 nm. All samples were

diluted by a constant dilution factor because the measuring method used had a maximum measurable concentration of 5 mg/L (American Public Health Association *et al.* 2017). The pH was measured using a pH meter (WTW inoLab pH 720, Xylem Inc., Germany).

3. RESULTS AND DISCUSSION

3.1. nZVI/AC characterization

3.1.1. SEM and EDX analysis

The overall micro-image of the synthesized nZVI/AC is shown in Figure 2(a). It seems that the nZVI particles formed small aggregates and were heterogeneously dispersed into the pores and cracks of the activated carbon. The occurrence of this aggregation was attributed to high surface energy and active magnetic interactions between the iron particles (Fu *et al.* 2013). However, the activated carbon played an important role in reducing the oxidation of the nZVI particles and preventing them from forming chain-like agglomerations (Liu *et al.* 2014). The activated carbon looked like a thin film while the iron particles were the round-shaped particles stabilized on activated carbon films as shown in Figure 2(b). The nZVI particles average size were roughly lower than 50 nm.

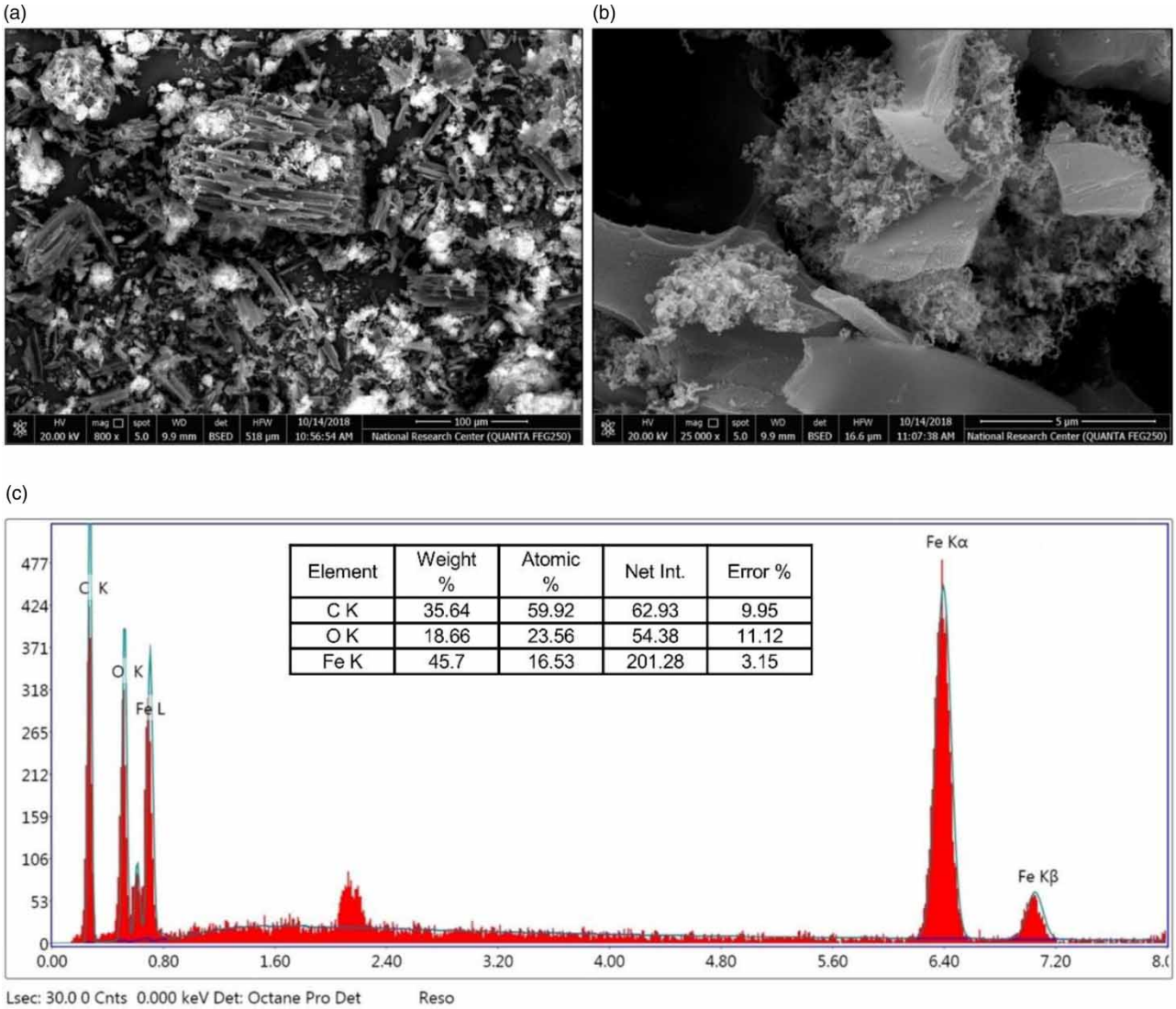

Figure 2 | SEM micro-images of nZVI/AC with resolutions of (a) 100 μm, (b) 5 μm, and (c) EDX spectrum of a randomly selected area in the nZVI/AC sample.

The EDX spectrum of a randomly selected area on the solid surface is shown in Figure 2(c), and reveals the presence of carbon, oxygen, and iron in the nZVI/AC sample with 35.64, 18.66, and 45.7%, respectively. The iron particles exist with the largest weight in this area, while the presence of small amounts of oxygen suggests that the nZVI particles were partially oxidized, but still have a large number of active sites (Li *et al.* 2017).

3.1.2. XRD, BET SSA, FTIR, and TGA

The XRD spectra of the nZVI/AC sample are shown in Figure 3(a). The diffraction peaks (2θ) found between 20–30° and 43–45° were attributed to the amorphous carbonaceous structure of the organic matrix and the zero-valent iron, respectively (Cao & Harris 2010; Yan *et al.* 2015). The analyzed nZVI/AC sample revealed the presence of a major peak of zero-valent iron (Fe^0) at $2\theta = 44.58°$ which confirms the formation of nanoscale iron particles in our sample. However, the diffraction peaks between 20 and 30° were weak, suggesting that the organic components mostly reacted with nZVI as stated by Qian (Qian *et al.* 2017).

The mesoporous structure of the nZVI/AC sample was studied, and textural properties were estimated from nitrogen adsorption and desorption isotherms (see Figure 3(b)). The isotherms of nZVI/AC showed a typical type II isotherm hypothesis curve, which indicates the presence of a typical mesoporous structure according to the IUPAC classification (Mulik *et al.* 2008). The surface area of the nZVI/AC samples was determined using the multipoint BET model. Under optimized synthesis conditions, the nZVI/AC particles exhibited BET SSA values of 72.6558 m^2/g; this was greater than the values reported by other studies in the literature, where the BET SSA values were 46.27 m^2/g for nZVI (Hwang *et al.* 2011), 36.5 m^2/g for nZVI (Liu *et al.* 2004), 29.8 m^2/g for nZVI/pillared clay (Zhang *et al.* 2011), and 25 m^2/g for nZVI (Yuvakkumar *et al.* 2011). The pore size was determined using the Barret–Joyner–Halenda (BJH) and Dollimore–Heal (DH) adsorption and desorption methods. The average pore size was 2.325 nm, which falls within the mesopore range according to the IUPAC classification. The average particle diameter was 37 nm, which was consistent with the SEM analysis.

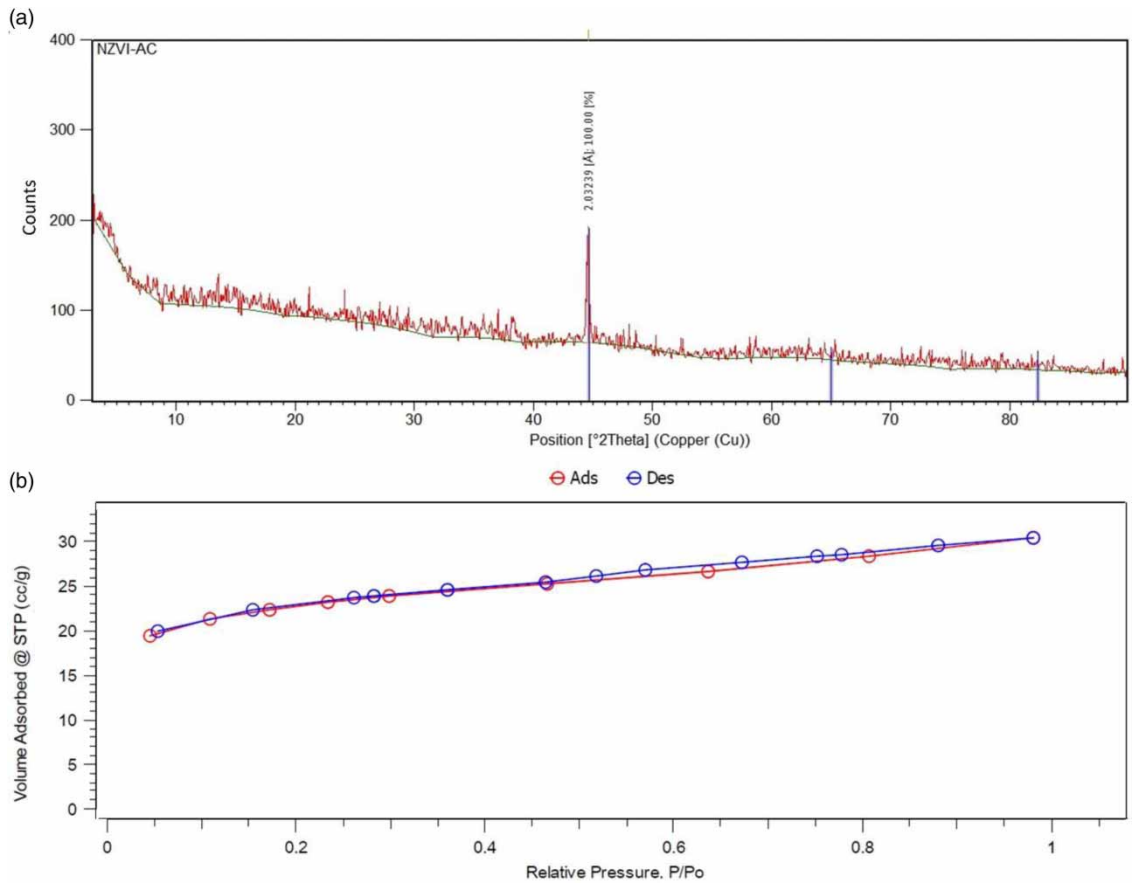

Figure 3 | (a) XRD pattern of the nZVI/AC sample, and (b) Nitrogen adsorption (Ads)–desorption (Des) isotherms of nZVI/AC.

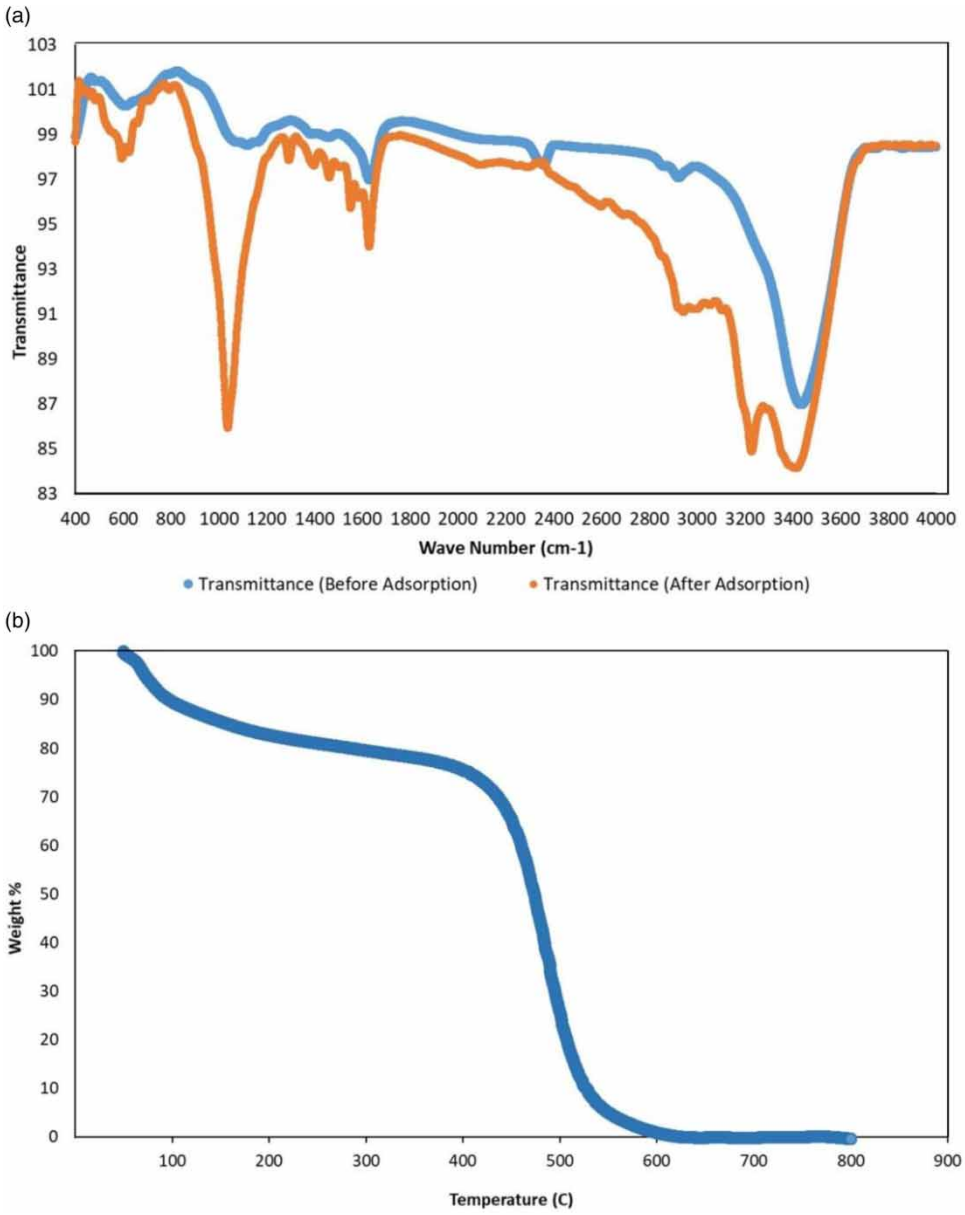

Figure 4 | (a) FTIR spectra of the nZVI/AC samples before and after phosphorus adsorption, and (b) TGA of the nZVI/AC sample.

The FTIR spectra of the nZVI/AC before and after phosphorus adsorption are shown in Figure 4(a). The FTIR data before the adsorption process revealed that the wide transmittance around a peak of 3,434 cm^{-1} was due to the stretching vibration of the O–H groups, as well as H-bonding, which was a common characteristic that indicates the adsorption of molecular water (Gosu *et al.* 2016). A broad transmittance region between 458 and 1,042 cm^{-1} was found to be caused by iron oxides and could be attributed to the stretching vibration of Fe–O, which confirms the presence of nZVI on the activated carbon surface (Kahani & Jafari 2009; Li *et al.* 2010). After phosphorus adsorption, the presence of sharp bands at 3,229 and 3,412 cm^{-1} may be attributed to the presence of molecular water. There was a clear peak at 1,631 cm^{-1} which was attributed to the stretching vibrations of carboxylate (C–C) and amide (C–N) complexes (Qian *et al.* 2017). A new sharp peak also appeared at 1,038 cm^{-1}. This peak could be attributed to the formation of (P–O–Fe) complexes between the phosphorus and iron oxides (Lǔ *et al.* 2013; Yoon *et al.* 2014).

The TGA curve of the nZVI/AC sample, shown in Figure 4(b), revealed how functional groups broke down on the surface of the sample. The first stage occurred below 100 °C, where there was a weight loss of about 10%; this was attributed to the

desorption of water. The second stage occurred in the temperature range between 100 and 420 °C, where the sample experienced a 17% loss in weight; this can be attributed to the decomposition of carboxylate groups on the surface of the sample. The third stage occurred between 420 °C and approximately 620 °C, where there was a rapid drop in weight until the complete decomposition of iron oxides complexes on the sample. The significant weight loss observed during the TGA analysis assured the presence of Fe–O functional groups on the nZVI/AC particles surface, while this rapid drop did not occur for AC particles alone as indicated in previous studies (Saleh *et al.* 2017; Safwat & Matta 2018).

3.2. Results of the batch experiments

The rate of phosphorus removal appeared to be faster under aerobic conditions compared to anaerobic conditions (Figure 5(a)). Both experiments achieved the same removal efficiency of approximately 70%. Aerobic conditions exposed the nanoscale iron surface to air, leading to increased iron corrosion, which in turn assisted the adsorption of phosphorus because ferric oxides/hydroxides are efficient sorbents for contaminants. During the adsorption process, phosphorus ions can replace hydroxyl ions (OH^-) on the surface of ferric oxides/hydroxides, forming inner-sphere complexes (Yoon *et al.* 2014; Eljamal *et al.* 2016).

As shown in Figure 5(b), the efficiency of phosphorus removal decreased as the initial pH value increased from 3 to 9. Samples extracted from the solution after 90 min showed that the phosphorus removal efficiency decreased from 78% to 44% when the pH value of the solution was raised. The isoelectric point (IEP) of nZVI/AC was found to be pH 7.6 (Zhu *et al.* 2009; Khalil *et al.* 2018). The pH value of the solution affects the electric charge of the surface of the nZVI/

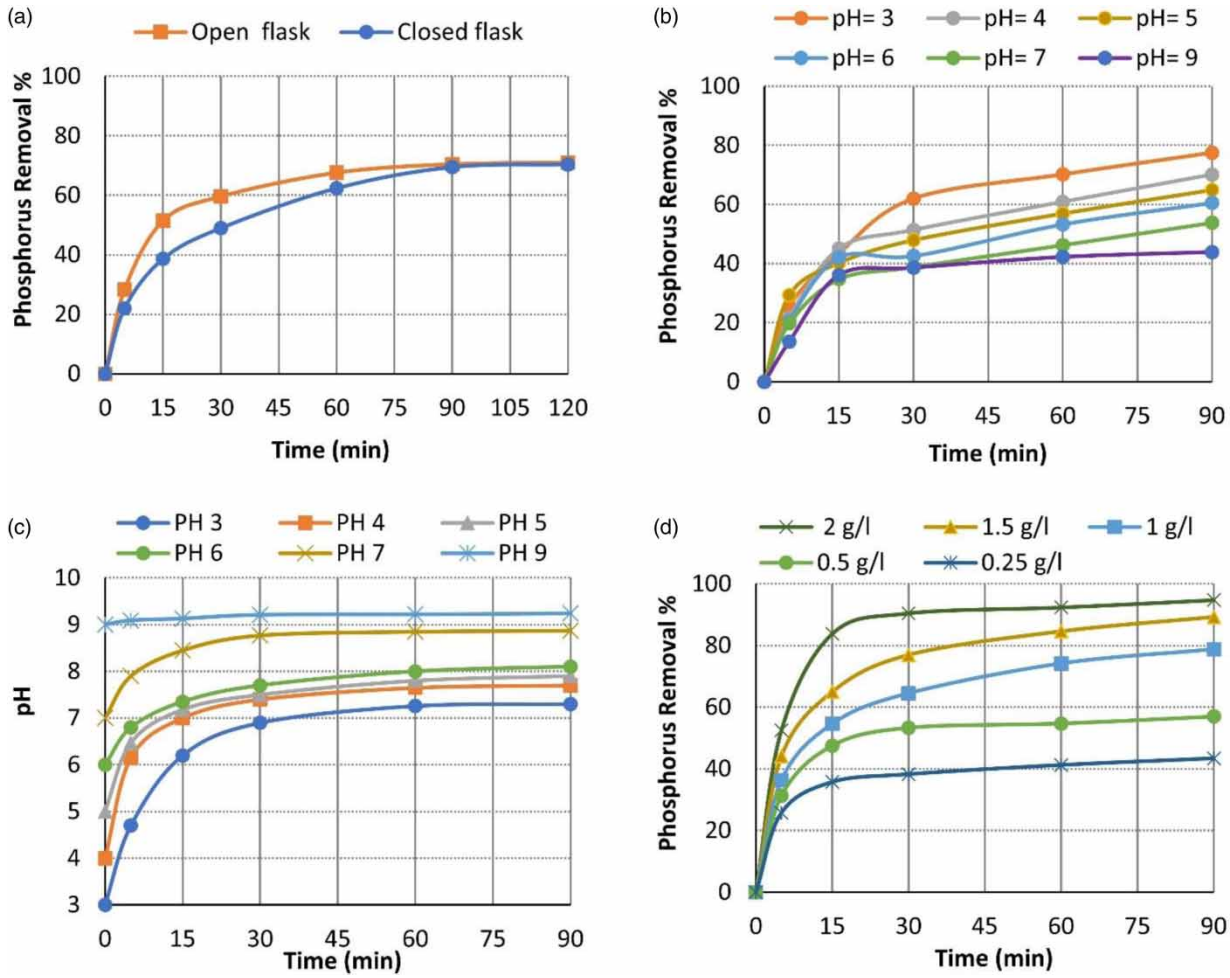

Figure 5 | The effects of (a) air presence, and (b) initial pH on phosphorus removal. (c) Variation in the pH of the solution during the adsorption process. (d) Effect of nZVI/AC dosage on phosphorus removal.

AC particles. The particles surface charge is positive at pH values below the IEP and negative at pH values above IEP. This leads to an increase in electrostatic attraction or repulsion with the anionic phosphorus species, and as a result, more and less readily adsorbs phosphorus, respectively (Zhu *et al.* 2009). Moreover, the nZVI/AC surface would be more readily protonated under acidic conditions, which promotes the complexation reaction (coagulation process) between Fe–OH^+ and the phosphorus species, forming outer-sphere complexes which may be further removed by co-precipitation processes (He *et al.* 2018).

Most of the active sites on the surface of nZVI/AC carried negative charges when under alkaline conditions, causing electrostatic repulsion with phosphate ions. Moreover, there were more hydroxide ions in the solution which competed with the phosphorus ions for the adsorption sites (Wen *et al.* 2014). This explains the significantly decreased phosphorus removal efficiency when solution pH was 9. The adsorption of phosphorus decreased with increasing solution pH; this was consistent with previous studies of phosphorus adsorption on nZVI (Mezenner & Bensmaili 2009; Almeelbi & Bezbaruah 2014; Yoon *et al.* 2014).

As the phosphorus adsorption process progressed, the pH of the solution increased as the nanoscale iron particles on the surface of the nZVI/AC composite were corroded into ferrous and ferric oxides/hydroxides in the solution (He *et al.* 2018). The solubility of iron particles depends on the pH of the solution. Highly acidic and highly alkaline conditions increase the solubility of iron particles, which result in increased pollution. A pH range between 7 and 8 was ideal to ensure the insolubility of iron particles (Schwertmann 1991). The variation in the pH of the solution was examined during the progress of the phosphorus adsorption process as shown in Figure 5(c). It was observed that initial solutions that were more acidic tended to reach a final pH range that prevented the solubility of iron particles. This result indicates that nanoscale iron particles were efficient for removing phosphorus while not resulting in any unfavorable iron pollution. A pH value of 4 was selected for the following batches as it achieved an adequate phosphorus removal efficiency. It was chosen in favor of pH 3, which required a large amount of 0.1 M HCL solution for pH adjustment.

As shown in Figure 5(d), the removal efficiency of phosphorus increased from 43% to 95% as the nZVI/AC dose was increased from 0.25 to 2.0 g/L. This suggests that using high adsorbent doses increases the availability of active sites for adsorption (Wu *et al.* 2013b). The nZVI/AC dosage of 1.0 g/L was used in all the following experiments as it achieved an acceptable removal efficiency of 79% with a reasonable amount of adsorbent. Increasing the nZVI/AC dosage to 1.5 and 2 g/L achieved higher removal efficiencies of 89 and 95%, respectively, which were not considered to be significantly higher than the removal efficiency achieved by the 1.0 g/L dose. Increasing the dose of nZVI/AC from 0.5 to 1 g/L increased the removal efficiency significantly from 57 to 79%, which is consistent with previous studies (Mezenner & Bensmaili 2009; Wu *et al.* 2013b).

Figure 6(a) shows that the removal efficiency increased from 77 to 85% when the rotation speed was increased from 100 to 250 rpm. These results indicate that the effect of rotation speed was not as significant as similar results were achieved at all rotation speeds, even after 60 min. A rotation speed of 200 rpm was selected for the following batches as it achieved a good removal efficiency of 83% which was very close to the removal efficiency of 85% achieved at 250 rpm. A rotation speed of 200 rpm was also selected in previous works (Wen *et al.* 2014; Eljamal *et al.* 2016).

Figure 6(b) shows that an increase in initial phosphorus concentration results in a decrease in phosphorus removal efficiency. As the initial phosphorus concentration increased from 20 to 50 mg P/L, the phosphorus removal efficiency decreased from 100 to 83% after 5 h. The phosphorus removal rate was observed to be rapid in the first 30 min, following which there was a decrease in the removal rate until equilibrium was reached. These results suggest that the ratio of the adsorbate molecules to the vacant active sites of the adsorbent greatly affects the removal efficiency of the adsorption process (Soliemanzadeh & Fekri 2017). At the beginning of each experiment, all of the active sites on the nano particles surface were vacant, which explains the rapid rate of removal in the first 30 min. Over time, the vacant active sites of the adsorbent became saturated with phosphorus ions, leading to an increase in the aforementioned ratio and decreasing the efficiency of phosphorus removal. Furthermore, as the adsorption process progresses, any remaining vacant active sites become less available to phosphorus ions due to repulsive forces between the phosphorus ions adsorbed on the surface of the adsorbent and the bulk phase; this explains the decrease in the removal rate after the first 30 min (Mezenner & Bensmaili 2009). Hence, the removal efficiency worsens as the phosphorus initial concentration is increased, assuming the nZVI/AC dosage remains constant (Wu *et al.* 2013b; Gosu *et al.* 2016).

Figure 6(c) shows that increasing the temperature from 15 to 37 °C led to an increase in the phosphorus removal efficiency from 76 to 86% after 3 h, suggesting that the adsorption process was endothermic (Boparai *et al.* 2011). It was also observed that the equilibrium was obtained after 3 h at experimental temperatures of 26 and 37 °C. In contrast, the phosphorus removal

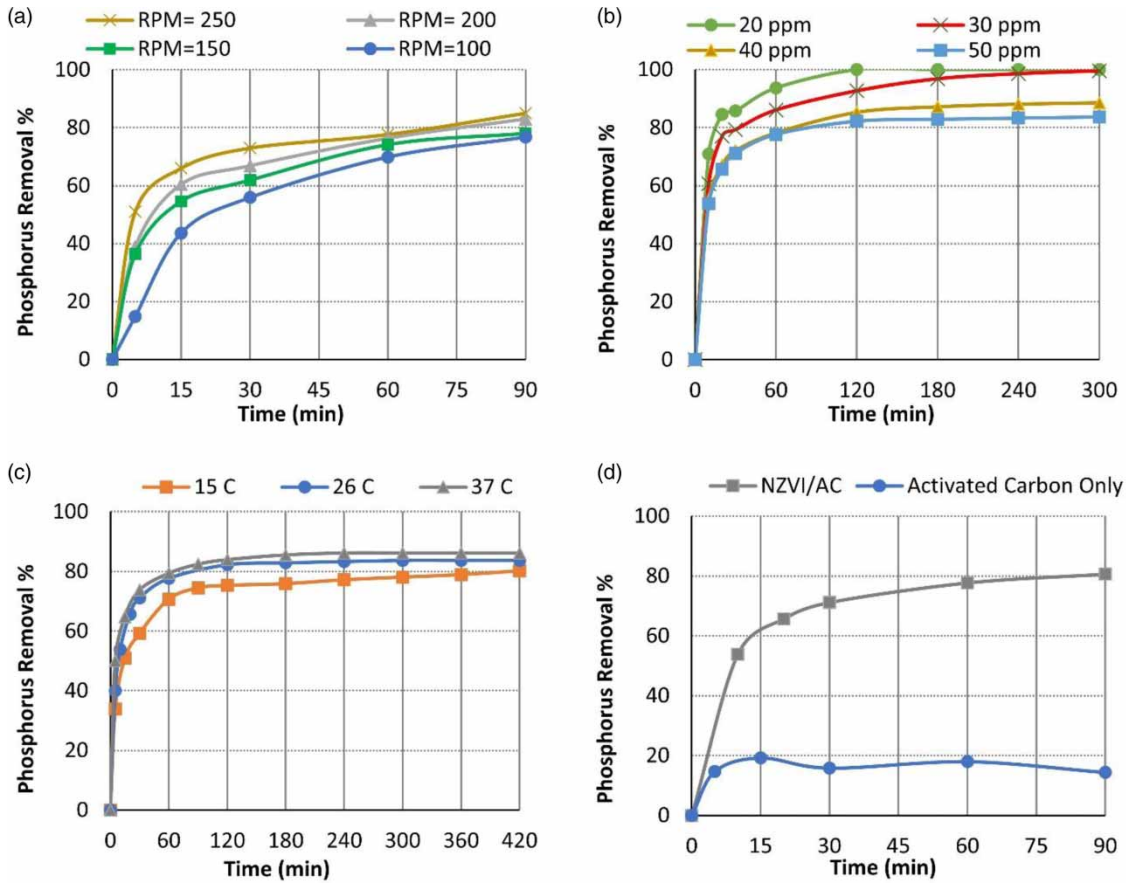

Figure 6 | The effects of (a) rotation speed, (b) initial phosphorus concentration as P, and (c) temperature on phosphorus removal. (d) Performance of activated carbon for phosphorus removal.

rate was slow in the experiment conducted at 15 °C compared to those conducted at higher temperatures. This suggests that increasing the temperature results in the excitation of phosphorus molecules, increasing their mobility from the bulk solution to the surface of the nZVI/AC (Gosu *et al.* 2016).

The comparison between the performance of AC and nZVI/AC was carried out under the same conditions. Figure 6(d) shows that the performance of activated carbon was poor compared to nZVI/AC. The adsorption capacity of AC was low relative to the nZVI/AC particles. The removal efficiency of AC reached nearly 19% after 15 min, following which the removal efficiency dropped to 15% after 2 h. This indicates that the AC was unable to retain the phosphorus ions adsorbed on its surface, while nZVI could form complexes between iron oxides and phosphorus ion species (Lǔ *et al.* 2013). Hence, based on these results, AC cannot be considered to be an appropriate choice for the removal of phosphorus ion species. There are no records in the literature of AC being used for the removal of phosphorus.

3.3. Adsorption isotherm, kinetics, and adsorption mechanisms

The adsorption of phosphorus on nZVI/AC particles was analyzed using four isotherms models as described in the Materials and Methods section. After nearly 180 min, the phosphorus uptake did not change further, implying that a contact time of 180 min was enough to reach the adsorption equilibrium. The phosphorus equilibrium uptake values (q_e) of nZVI/AC at different initial concentrations of 20, 30, 40, and 50 mg/L were estimated to be 18.96, 28.32, 33.58, and 39.66 mg/g, respectively (Equation (3)). These values were used to plot the adsorption isotherm and fitted to the kinetic models.

The correlation coefficients (R^2) of the Freundlich, Langmuir, Temkin, and D–R equations were 0.95, 0.99, 0.87, and 0.71, respectively (see Table 2). This indicates that phosphorus adsorption by nZVI/AC was best fitted by the Langmuir equation, which shows that the phosphorus ions adsorption process by nZVI/AC can be described as the monolayer adsorption of ions onto energetically homogeneous surfaces with a finite number of adsorption sites (Boparai *et al.* 2011). The calculated

Table 2 | Isotherm model parameters and correlation coefficients for phosphorus adsorption on nZVI/AC particles at different initial concentrations

Isotherm model	Parameter	Value
Freundlich	K_F	33.81
	n	11.39
	R^2	0.95
Langmuir	q_m (mg/g)	53.76
	K_L (l/mg)	0.46
	R^2	0.99
Temkin	b (J/mol)	892.34
	K_T (l/gm)	370,869.46
	R^2	0.87
Dubinin–Radushkevich	q_d (mg/g)	39.86
	β (mol/kJ)^2	0.0026
	R^2	0.71

isotherm parameters for phosphorus removal by nZVI/AC are summarized in Table 2. The Freundlich isotherm model constants K_F and n were determined from the slope and intercept of a plot of log q_e against log C_e (Supplementary Material, Figure S-1(a)). The value of n was determined to be 11.39, which was greater than unity indicating a system that favored chemical adsorption. Isotherms with high n values ($n > 1$) indicate the presence of a chemisorption process and are categorized as L-type isotherms, which suggests that there is a high affinity between the adsorbent and adsorbate (Huat *et al.* 2004).

From the Langmuir model (Supplementary Material, Figure S-1(b)), the maximum phosphorus adsorption capacity (q_m) was estimated to be 53.76 mg P/g. This was much higher than the adsorption capacity reported for previously studied adsorbents: nZVI/Bentonite gives 27.63 mg P/g (Soliemanzadeh & Fekri 2017), nZVI/Graphene gives 14.71 mg P/g (Liu *et al.* 2014), iron hydroxide-eggshell waste gives 14.49 mg P/g (Mezenner & Bensmaili 2009) and magnetic iron oxide nanoparticles gives 5.03 mg P/g (Yoon *et al.* 2014). The linear plot of the Temkin adsorption isotherm (Supplementary Material, Figure S-1(c)), which considers the chemisorption of an adsorbate onto the adsorbent (Biswas *et al.* 2007); the data were found to fit this model rather well ($R^2 = 0.87$). This supports our interpretation that phosphorus adsorption onto nZVI/AC is a chemisorption process. The D–R adsorption isotherm parameters were determined from the slope and intercept of the plotted line (Supplementary Material, Figure S-1(d) and Table 2). The maximum coverage value ($q_d = 39.86$ mg/g) was not consistent with the q_m value (53.76 mg/g) previously determined from the Langmuir isotherm. The correlation coefficient for the D–R isotherm was the lowest compared to the other isotherm models (Table 2). This suggests that the phosphorus adsorption onto nZVI/AC particles was not a physical process.

The study of adsorption kinetics is critical in evaluating the effectiveness of the adsorption process. Moreover, it is essential to determine the type of adsorption process in a given system (Mezenner & Bensmaili 2009). In this study, three models were applied to describe the sorption kinetics of phosphorus on nZVI/AC particles as described in the Materials and Methods section. The adsorption kinetics models for phosphorus removal by nZVI/AC are summarized in Table 3 (Supplementary Material, Figure S-2). The correlation coefficients (R^2) indicate that the pseudo-second-order model was the best fit for the kinetic data. These results suggest that the adsorption of phosphorus onto the nZVI/AC nanoparticles occurred via a

Table 3 | Kinetic models parameters and correlation coefficients for phosphorus adsorption on nZVI/AC particles at different initial concentrations

Initial Conc. (mg/L)	$q_{e,exp.}$ (mg/g)	Pseudo-first-order K_1 (1/h)	Pseudo-second-order $q_{e,cal.}$ (mg/g)	Elovich equation R^2	Initial Conc. (mg/L)	$q_{e,exp.}$ (mg/g)	Pseudo-first-order K_1 (1/h)	Pseudo-second-order $q_{e,cal.}$ (mg/g)	Elovich equation R^2	Initial Conc. (mg/L)
50	39.66	1.1139	11.03	0.9591	0.214	40.49	350.77	1	30,182.5	0.2559
40	33.58	1.0617	11.94	0.9934	0.227	34.48	269.92	0.9999	1,1296.81	0.2784
30	28.32	0.8759	10.04	0.9872	0.238	28.99	199.96	0.9997	9,240.31	0.3332
20	18.96	1.3632	4.71	0.9581	0.502	19.72	195.28	0.9995	9,218.84	0.4731

chemisorption process (Ho 2006; Tu & You 2014). The parameters of the pseudo-second-order model (Table 3) indicate that the phosphorus adsorption capacity (q_e) increased as the initial concentration increased; this is consistent with the findings of previous studies (Mezenner & Bensmaili 2009; Yoon *et al.* 2014; Soliemanzadeh & Fekri 2017).

The values of k_2 shown in Table 3 decreased as the initial phosphorus concentration increased, implying that the required time to reach equilibrium increased as the initial phosphorus concentration increased. The values of h also increased with increasing initial phosphorus concentration, implying that adsorption at the initial stage of the adsorption became faster with increasing initial concentration. The initial adsorption rate constant (α) from the Elovich model led to the same conclusion but with different orders of magnitude (Yoon *et al.* 2014). These results indicate that the chemisorption mechanism may play a significant role in the adsorption of phosphorus on nZVI/AC particles (Mezenner & Bensmaili 2009). The calculated equilibrium adsorption capacity ($q_{e,cal.}$) values were closer to the experimental ($q_{e,exp.}$) values for the pseudo-second-order model than for the pseudo-first-order model (Table 3), which confirms that the pseudo-second-order model better describes the phosphorus adsorption on nZVI/AC particles.

The Elovich equation coefficients, β and α, were determined from the slope and intercept of the linear graph plotted between q_t and $\ln(t)$, respectively (Supplementary Material, Figure S-2(c)). The values of α and β varied as a function of the initial phosphorus concentration (Table 3). Therefore, by increasing the initial phosphorus concentration from 20 to 50 mg/L, the value of β (the extent of surface coverage) decreased from 0.473 to 0.256 g/mg due to the surface being less readily available for phosphorus adsorption. In contrast, an increase in the initial phosphorus concentration from 20 to 50 mg/L leads to an increase in the value of α (initial adsorption rate) from 9,218.84 to 30,182.5 mg/g h (Mezenner & Bensmaili 2009).

The previously mentioned kinetic models could not distinguish the diffusion mechanism and rate-controlling steps associated with the adsorption phenomena. Therefore, the Weber–Morris intra-particle diffusion model was applied to determine whether intra-particle diffusion was the rate-limiting step, as described in Equation (12) (Weber 1963):

$$q_t = K_i * t^{1/2} + C \tag{12}$$

where K_i is the intra-particle diffusion rate constant (mg/g $h^{1/2}$) and C (mg/g) is a constant which is associated with the thickness of the boundary layer (Mezenner & Bensmaili 2009). The intra-particle diffusion model plots for the adsorption of phosphorus on nZVI/AC particles (Supplementary Material, Figure S-2(d)). The plots can be divided into three linear sections, which supposes that the adsorption process carried out in three steps. The initial steeper section is usually attributed to surface diffusion effects. The second linear section defines the gradual adsorption stage, where pore diffusion is rate-limiting. The third section is associated with the final adsorption equilibrium stage where pore diffusion slows down as the equilibrium is reached (Boparai *et al.* 2011; Safwat & Matta 2018). As the plots at each concentration did not pass through the origin, pore diffusion is not the only rate-limiting step. This analysis revealed that the three processes control the adsorption rate, but further investigation was required to identify the rate-limiting step (Soliemanzadeh & Fekri 2017).

The intra-particle diffusion rate constant (K_i) and the intercept (C) were calculated from the slope of the second linear section (Boparai *et al.* 2011). The intercept values increased from 14.85 to 31.59 mg/g as the initial concentration was increased from 20 to 50 mg/L. The larger intercept values indicate that surface diffusion has a greater effect as the rate-limiting step (Soliemanzadeh & Fekri 2017). It was also observed that the K_i values increased as the initial phosphorus concentration was increased. This can be attributed to the growing effect of driving force which reduces the diffusion of phosphorus ions in the outer layer and enhances the diffusion of phosphorus into the internal pores (Mezenner & Bensmaili 2009).

To determine whether the surface diffusion or pore diffusion was the slowest step in the adsorption of phosphorus ions, the Boyd kinetic model (Equation (13)), was applied which define the actual rate-limiting step involved in the adsorption process (Safwat & Matta 2018):

$$Bt = -0.4977 - \ln\left(1 - \frac{q_t}{q_e}\right) \tag{13}$$

where Bt is a mathematical function of q_t/q_e. The Boyd kinetic model plots (Supplementary Material, Figure S-2(e)) were linear but do not pass through the origin for all studied initial concentrations; this suggests that the rate of the phosphorus adsorption on nZVI/AC particles is primarily governed by surface diffusion (Senthilkumar *et al.* 2012).

3.4. Thermodynamic investigation

A thermodynamic study was used to provide a more detailed description of the adsorption process. Experiments of phosphorus adsorption onto nZVI/AC particles were carried out at temperatures ranging from 288 to 310 K with an initial phosphorus concentration of 50 mg/L, pH 4, and a fixed adsorbent dose of 1 g/L. The data obtained were used to study the thermodynamics of phosphorusdsorption.

The thermodynamic equilibrium constant or thermodynamic distribution coefficient (K_o) of the adsorption process was derived by plotting ln (q_e/C_e) against C_e and extrapolating C_e to zero (Supplementary Material, Figure S-3(a)), as proposed by Khan and Singh (Khan & Singh 1987; Adam & Chua 2004). The standard Gibbs free energy change $\Delta G°$ (kJ/mol) was then determined using Equation (14). The standard enthalpy change $\Delta H°$ (kJ/mol) and standard entropy change $\Delta S°$ (J/mol K) were calculated from the slope and intercept of the plot of ln(K_o) against $1/T$ (Supplementary Material, Figure S-3(b)), respectively, using Equation (15) (Yan *et al.* 2010; Tu & You 2014).

$$\Delta G^o = -RT \ln K_o \tag{14}$$

$$\ln K_o = \frac{\Delta S^o}{R} - \frac{\Delta H^o}{RT} \tag{15}$$

where R is the universal gas constant (8.314 J/mol K) and T is the temperature of the solution (K).

Table 4 shows that K_o increase with temperature implying that the process was endothermic. Negative values of $\Delta G°$ reveal that the process was spontaneous. The values of $\Delta G°$ decrease from −21.87 to −24.12 kJ/mol as the temperature increases from 288 to 310 K, which indicates that the spontaneity of the adsorption process increased as temperatures increased (Mezenner & Bensmaili 2009; Tu & You 2014). Furthermore, the positive standard enthalpy change ($\Delta H°$) of 7.65 kJ/mol for this process proves that the adsorption of phosphorus by nZVI/AC particles was endothermic, which is consistent with the enhanced phosphorus adsorption at high temperatures. The positive standard entropy change ($\Delta S°$) of 102.52 J/mol K reflects the affinity of the phosphorus ions for nZVI particles and the increasing randomness at the solid–solution interface during the phosphorus adsorption onto nZVI/AC particles (Boparai *et al.* 2011). These results were consistent with previous studies of phosphorus adsorption on magnetic iron oxide nanoparticles (Yoon *et al.* 2014), phosphorus adsorption on iron hydroxide-eggshell waste (Mezenner & Bensmaili 2009), phosphorus adsorption onto nZVI, and phosphorus adsorption on green synthesized nano-bimetal ferrites (Tu & You 2014; Maamoun *et al.* 2021).

3.5. Interference studies

The studied interference effects involved cations, anions, the hardness of the solution, and the presence of organic matter. The cation batches revealed that the presence of cations enhanced the adsorption capacity of phosphorus and its rate of adsorption on nZVI/AC particles (Figure 7(a)). The $CaCl_2$ batch reached 100% removal efficiency after only 120 min, while the removal efficiency of the phosphorus control batch was 81.5% and only reached 83% after 180 min. In addition, the $NiCl_2$, $CuSO_4$, and NaCl compounds also improved the phosphorus adsorption capacity, and their removal efficiencies were 95.5, 93.7, and 89.9% after 120 min, respectively.

The cations improved the phosphorus removal efficiency because they stimulated and increased iron corrosion on the surface of nZVI particles. This occurs because the metal cations tend to be reduced to their metals. Consequently, the zero-valent iron was converted to iron ions (Fe^{2+} and Fe^{3+}). These iron ions were oxidized to ferrous and ferric oxides/hydroxides, which are good absorbents of phosphorus (Eljamal *et al.* 2016; Khalil *et al.* 2016). The concentration of the cation and its charge control the extent to which the cations enhance the phosphorus removal efficiency. As the concentration or the charge of the cation increases, the aforementioned enhancing effect becomes more pronounced. Hence, $CaCl_2$ (500 mg/L) had a

Table 4 | Thermodynamic parameters for phosphorus adsorption onto nZVI/AC particles

Temperature (K)	K_o (kg^{-1})	$\Delta G°$ (kJ/mol)	$\Delta H°$ (kJ/mol)	$\Delta S°$ (J/mol K)
288	9,247.01	−21.87	7.65	102.52
299	10,472.99	−23.01		
310	11,599.94	−24.12		

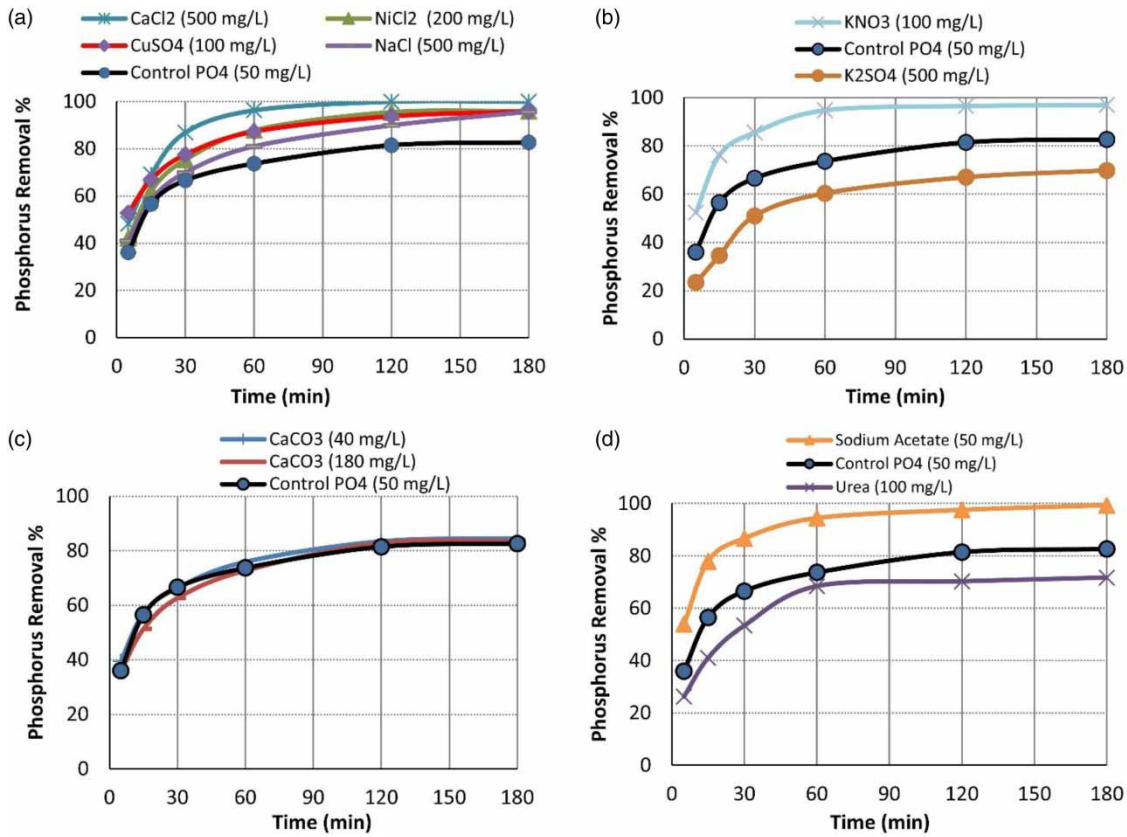

Figure 7 | The interference effects on the phosphorus removal efficiency of nZVI/AC: (a) cations, (b) anions, (c) hardness, and (d) organic matters.

more pronounced enhancing effect than $NiCl_2$ (200 mg/L): despite both cations having the same +2 charge solely due to the difference in concentration. The $CuSO_4$ (100 mg/L) had a better adsorption rate than NaCl (500 mg/L), although they exhibited similar adsorption capacities after 180 min. This showed that the higher charge of copper ion (+2) with a lower concentration of 100 mg/L resulted in a higher adsorption rate than the lower charge of the sodium ion (+1) with a higher concentration of 500 mg/L; this suggests that the charge of the cation plays a more significant role than the concentration of the cation (Khalil *et al.* 2018).

The anion studies revealed that the presence of nitrate ions (NO_3^-) enhanced the phosphorus adsorption capacity and adsorption rate on nZVI/AC particles. In contrast, the presence of sulfate ions (SO_4^{2-}) negatively affected phosphorus' adsorption capacity on nZVI/AC particles (Figure 7(b)). The KNO_3 batch achieved a 96.5% removal efficiency after 120 min, which was higher than the control batch that only reached an 81.5% removal efficiency, while the K_2SO_4 batch attained a removal efficiency of only 67%. The enhancing effect of the nitrate ions could be attributed to nitrate reduction by nZVI, which results in the oxidation and corrosion of iron and the formation of ferrous and ferric oxides that could have improved the phosphorus adsorption capacity and the kinetics of the reaction. However, the nitrate reduction by nZVI/AC particles resulted in a rapid increase in the pH of the solution, creating more negative charges on the surface of the nZVI/AC, which was unfavorable for the adsorption of phosphorus. Overall, the enhancement effects were higher than that of the inhibitory effects. Consequently, the presence of nitrate enhanced the phosphorus removal efficiency of nZVI/AC particles (Khalil *et al.* 2017; He *et al.* 2018). In contrast, SO_4^{2-} competed against the phosphate anions (PO_4^{3-}) to occupy the active sites on the surface of the nZVI/AC particles. This competition reduces the availability of the adsorbent surface for phosphorus adsorption, as can be seen in the phosphorus control batch; this results in a lower phosphorus removal rate and adsorption capacity as shown in Figure 7(b) (Khalil *et al.* 2017).

The batch experiments that investigated the effects of the hardness of the solution revealed that the presence of calcium carbonate slightly improved the phosphorus removal efficiency (Figure 7(c)). This could be attributed to the presence of

calcium ions (Ca^{2+}) that stimulate iron corrosion, leading to the formation of iron oxides/hydroxides, which are good adsorbents for phosphorus. However, the enhancing effect of the Ca^{2+} ions was inhibited by the carbonate anions (CO_3^{2-}), which compete with the phosphate anions (PO_4^{3-}) to occupy the active sites on the surface of the nZVI/AC particles. In the overall reaction, the enhancing effect of the presence of $CaCO_3$ was slightly higher than the inhibitory effect, resulting in a slight increase in phosphorus removal efficiency (Khalil *et al.* 2018). When the calcium carbonate concentration increased from 40 to 180 mg/L, the removal efficiency became slightly lower. This can be interpreted by the fact that the competition between the carbonate and phosphorus ions increased, while the nZVI/AC particle dose, and thus the number of active sites, remained constant and limited.

Studies on the presence of organic matter revealed that the presence of sodium acetate significantly enhanced the phosphorus adsorption capacity for nZVI/AC particles. In contrast, the presence of urea negatively affected the adsorption capacity (Figure 7(d)). The sodium acetate batch reached a 97.6% removal efficiency after 120 min, while the urea batch reduced the removal efficiency to 70.3%. The enhancing effect of sodium acetate could be attributed to the presence of sodium cations (Na^+) that stimulate iron corrosion, resulting in the formation of iron oxides which are good adsorbents for phosphorus. The negative effects of urea could be explained by urea functional groups competing with phosphate anions to occupy the active sites on the surface of the nZVI/AC particles. Hence, the phosphorus adsorption capacity and removal rate were inhibited in the urea batch (Almeelbi & Bezbaruah 2014).

4. CONCLUSION

In this study, nZVI/AC composite proved to be an efficient adsorbent for phosphorus with high removal efficiencies. The SEM analysis showed that the nZVI particles were well dispersed into the pores and cracks of the AC, while the EDX analysis showed that the main elements that exist on the solid surface are carbon, oxygen, and iron. XRD analysis confirmed the formation of nZVI particles with less oxidized iron products (Fe_2O_3). BET SSA was 72.66 m^2/g, suggesting a high surface area available for adsorption. FTIR analysis indicated the formation of (P–O–Fe) complexes after adsorption, proving that the phosphorus removal mechanism involved adsorption and co-precipitation. Batch experiments revealed that phosphorus removal rates were better under aerobic conditions due to rapid iron corrosion. Acidic pH values, specifically below IEP of nZVI/AC particles, greatly enhanced the phosphorus removal efficiency. Higher nZVI/AC dosages improved the adsorption capacity, while the shaker rotation speed effect did not affect the phosphorus removal efficiency. Higher initial phosphorus concentrations led to a decrease in the phosphorus removal rate.

Langmuir adsorption isotherm model best fitted the adsorption results. Accordingly, phosphorus adsorption could be well-described by the monolayer adsorption of ions on energetically homogeneous surfaces. The maximum phosphorus adsorption capacity (q_m) was estimated to be 53.76 mg/g. The adsorption kinetics was best described by the pseudo-second-order kinetic model confirming a chemisorption process. Boyd kinetic model revealed that the surface diffusion was the slowest stage in phosphorus adsorption on nZVI/AC particles. Thermodynamic analysis indicated that the adsorption process was endothermic, spontaneous and that the spontaneity degree increased with increasing temperature. Interference studies showed that the presence of metallic salts, nitrate ions and sodium acetate had enhanced phosphorus removal efficiency, while the presence of sulfate ions and urea have reduced it during wastewater treatment. Therefore, it is highly recommended to utilize nZVI/AC particles in the presence of metallic salts for enhanced tertiary treatment in WWTPs with low retention time due to high removal rate. For future work, a typical domestic wastewater should be tested with nZVI/AC particles to understand its influence on the wastewater contaminants specially phosphorus. This study represents important participation and a perceptible conclusion to the recognition of the underlying interactions within the phosphorus removal process by nZVI/AC particles.

CONFLICTS OF INTEREST

The authors declare that they have no conflicts of interest.

DATA AVAILABILITY STATEMENT

All relevant data are included in the paper or its Supplementary Information.

REFERENCES

Adam, F. & Chua, J. H. 2004 The adsorption of palmytic acid on rice husk ash chemically modified with Al(III) ion using the sol-gel technique. *Journal of Colloid and Interface Science* **280**, 55–61. https://doi.org/10.1016/j.jcis.2004.07.006.

Almeelbi, T. & Bezbaruah, A. 2014 Aqueous phosphate removal using nanoscale zero-valent iron. In: *Nanotechnology for Sustainable Development, First Edition*, pp. 197–210. https://doi.org/10.1007/978-3-319-05041-6_16.

American Public Health Association, Baird, R., Eaton, A. D., Rice, E. W. & Bridgewater, L. & American Water Works Association, Water Environment Federation 2017 *Standard Methods for the Examination of Water and Wastewater*. American Public Health Association, Washington, DC.

Biswas, K., Saha, S. K. & Ghosh, U. C. 2007 Adsorption of fluoride from aqueous solution by a synthetic iron(III)-aluminum(III) mixed oxide. *Industrial and Engineering Chemistry Research* **46**, 5346–5356. https://doi.org/10.1021/ie061401b.

Boparai, H. K., Joseph, M. & O'Carroll, D. M. 2011 Kinetics and thermodynamics of cadmium ion removal by adsorption onto nano zerovalent iron particles. *Journal of Hazardous Materials* **186**, 458–465. https://doi.org/10.1016/j.jhazmat.2010.11.029.

Cao, X. & Harris, W. 2010 Properties of dairy-manure-derived biochar pertinent to its potential use in remediation. *Bioresource Technology* **101**, 5222–5228. https://doi.org/10.1016/j.biortech.2010.02.052.

Çelebi, O., Üzüm, Ç., Shahwan, T. & Erten, H. N. 2007 A radiotracer study of the adsorption behavior of aqueous Ba^{2+} ions on nanoparticles of zero-valent iron. *Journal of Hazardous Materials* **148**, 761–767. https://doi.org/10.1016/j.jhazmat.2007.06.122.

Elawwad, A. & Hazem, M. 2017 Minimization of sludge production in an integrated UASB-continuous flow sequencing batch reactor system. *Desalination and Water Treatment* **91**. https://doi.org/10.5004/dwt.2017.20643.

Elawwad, A., Naguib, A. & Abdel-Halim, H. 2016 Modeling of phenol and cyanide removal in a full-scale coke-oven wastewater treatment plant. *Desalination and Water Treatment* **57**. https://doi.org/10.1080/19443994.2016.1148637.

Eljamal, O., Khalil, A. M. E., Sugihara, Y. & Matsunaga, N. 2016 Phosphorus removal from aqueous solution by nanoscale zero valent iron in the presence of copper chloride. *Chemical Engineering Journal* **293**, 225–231. https://doi.org/10.1016/j.cej.2016.02.052.

Fu, F., Han, W., Huang, C., Tang, B. & Hu, M. 2013 Removal of Cr(VI) from wastewater by supported nanoscale zero-valent iron on granular activated carbon. *Desalination and Water Treatment* **51**, 2680–2686. https://doi.org/10.1080/19443994.2012.749328.

Gosu, V., Gurjar, B. R., Surampalli, R. Y. & Zhang, T. C. 2016 Treatment of pyridine-bearing wastewater by nano zero-valent iron supported on activated carbon derived from agricultural waste. *Desalination and Water Treatment* **57**, 6250–6260. https://doi.org/10.1080/19443994.2015.1005686.

He, Y., Lin, H., Dong, Y., Li, B., Wang, L., Chu, S., Luo, M. & Liu, J. 2018 Zeolite supported Fe/Ni bimetallic nanoparticles for simultaneous removal of nitrate and phosphate: synergistic effect and mechanism. *Chemical Engineering Journal* **347**, 669–681. https://doi.org/10.1016/j.cej.2018.04.088.

Ho, Y. S. 2006 Review of second-order models for adsorption systems. *Journal of Hazardous Materials* **136**, 681–689. https://doi.org/10.1016/j.jhazmat.2005.12.043.

Huat, B. B. K., Gue, S. S. & Ali, F. H. 2004 *Tropical Residual Soils Engineering*. A.A.Balkema Publishers. https://doi.org/10.1201/9780203024621.

Hwang, Y. H., Kim, D. G. & Shin, H. S. 2011 Mechanism study of nitrate reduction by nano zero valent iron. *Journal of Hazardous Materials* **185**, 1513–1521. https://doi.org/10.1016/j.jhazmat.2010.10.078.

Kahani, S. A. & Jafari, M. 2009 A new method for preparation of magnetite from iron oxyhydroxide or iron oxide and ferrous salt in aqueous solution. *Journal of Magnetism and Magnetic Materials* **321**, 1951–1954. https://doi.org/10.1016/j.jmmm.2008.12.026.

Khalil, A. M. E., Eljamal, O., Jribi, S. & Matsunaga, N. 2016 Promoting nitrate reduction kinetics by nanoscale zero valent iron in water via copper salt addition. *Chemical Engineering Journal* **287**, 367–380. https://doi.org/10.1016/j.cej.2015.11.038.

Khalil, A. M. E., Eljamal, O., Amen, T. W. M., Sugihara, Y. & Matsunaga, N. 2017 Optimized nano-scale zero-valent iron supported on treated activated carbon for enhanced nitrate and phosphate removal from water. *Chemical Engineering Journal* **309**, 349–365. https://doi.org/10.1016/j.cej.2016.10.080.

Khalil, A. M. E., Eljamal, O., Amen, T. W. M., Sugihara, Y. & Matsunaga, N. 2018 Scrutiny of interference effect of ions and organic matters on water treatment using supported nanoscale zero-valent iron. *Environmental Earth Sciences* **77**. https://doi.org/10.1007/s12665-018-7661-6.

Khan, A. A. & Singh, R. P. 1987 Adsorption thermodynamics of carbofuran on Sn (IV) arsenosilicate in H^+, Na^+ and Ca^{2+} forms. *Colloids and Surfaces* **24**, 33–42. https://doi.org/10.1016/0166-6622(87)80259-7.

Li, S., Wu, P., Li, H., Zhu, N., Li, P., Wu, J., Wang, X. & Dang, Z. 2010 Synthesis and characterization of organo-montmorillonite supported iron nanoparticles. *Applied Clay Science* **50**, 330–336. https://doi.org/10.1016/j.clay.2010.08.021.

Li, P., Lin, K., Fang, Z. & Wang, K. 2017 Enhanced nitrate removal by novel bimetallic Fe/Ni nanoparticles supported on biochar. *Journal of Cleaner Production* **151**, 21–33. https://doi.org/10.1016/j.jclepro.2017.03.042.

Li, X., Huang, L., Fang, H., He, G., Reible, D. & Wang, C. 2019 Immobilization of phosphorus in sediments by nano zero-valent iron (nZVI) from the view of mineral composition. *Science of The Total Environment* **694**, 133695. https://doi.org/10.1016/J.SCITOTENV.2019.133695.

Li, Q., Chen, Z., Wang, H., Yang, H., Wen, T., Wang, S., Hu, B. & Wang, X. 2021 Removal of organic compounds by nanoscale zero-valent iron and its composites. *Science of The Total Environment* **792**, 148546. https://doi.org/10.1016/J.SCITOTENV.2021.148546.

Liu, Y., Majetich, S. & Tilton, R. D. 2004 TCE dechlorination rates, pathways, and efficiency of two nanoscale iron particles. *Environmental Science and Technology* **39**, 1338–1345.

Liu, F., Yang, J. H., Zuo, J., Ma, D., Gan, L., Xie, B., Wang, P. & Yang, B. 2014 Graphene-supported nanoscale zero-valent iron: removal of phosphorus from aqueous solution and mechanistic study. *Journal of Environmental Sciences (China)* **26**, 1751–1762. https://doi.org/10.1016/j.jes.2014.06.016.

Lǔ, J., Liu, H., Liu, R., Zhao, X., Sun, L. & Qu, J. 2013 Adsorptive removal of phosphate by a nanostructured Fe-Al-Mn trimetal oxide adsorbent. *Powder Technology* **233**, 146–154. https://doi.org/10.1016/j.powtec.2012.08.024.

Ma, F., Zhao, B., Diao, J., Jiang, Y. & Zhang, J. 2020 Mechanism of phosphate removal from aqueous solutions by biochar supported nanoscale zero-valent iron. *RSC Advances* **10**, 39217–39225. https://doi.org/10.1039/D0RA07391A.

Maamoun, I., Eljamal, R., Falyouna, O., Bensaida, K., Sugihara, Y. & Eljamal, O. 2021 Insights into kinetics, isotherms and thermodynamics of phosphorus sorption onto nanoscale zero-valent iron. *Journal of Molecular Liquids* **328**, 115402. https://doi.org/10.1016/J.MOLLIQ.2021.115402.

Mezenner, N. Y. & Bensmaili, A. 2009 Kinetics and thermodynamic study of phosphate adsorption on iron hydroxide-eggshell waste. *Chemical Engineering Journal* **147**, 87–96. https://doi.org/10.1016/j.cej.2008.06.024.

Mulik, S., Sotiriou-Leventis, C. & Leventis, N. 2008 Macroporous electrically conducting carbon networks by pyrolysis of isocyanate-cross-linked resorcinol = formaldehyde aerogels. *Chemistry of Materials* **20**, 6985–6997. https://doi.org/10.1021/cm801428p.

Panagopoulos, A. 2021 Beneficiation of saline effluents from seawater desalination plants: fostering the zero liquid discharge (ZLD) approach – a techno-economic evaluation. *Journal of Environmental Chemical Engineering* **9**, 105338. https://doi.org/10.1016/J.JECE.2021.105338.

Qian, L., Zhang, W., Yan, J., Han, L., Chen, Y., Ouyang, D. & Chen, M. 2017 Nanoscale zero-valent iron supported by biochars produced at different temperatures: synthesis mechanism and effect on Cr(VI) removal. *Environmental Pollution* **223**, 153–160. https://doi.org/10.1016/j.envpol.2016.12.077.

Renu, Agarwal, M. & Singh, K. 2017 Heavy metal removal from wastewater using various adsorbents: a review. *Journal of Water Reuse and Desalination* **7**, 387–419. https://doi.org/10.2166/WRD.2016.104.

Safwat, S. M. & Matta, M. E. 2018 Adsorption of urea onto granular activated alumina: a comparative study with granular activated carbon. *Journal of Dispersion Science and Technology* **39**, 1699–1709. https://doi.org/10.1080/01932691.2018.1461644.

Saleh, T. A., Naeemullah, Tuzen, M. & Sarı, A. 2017 Polyethylenimine modified activated carbon as novel magnetic adsorbent for the removal of uranium from aqueous solution. *Chemical Engineering Research and Design* **117**, 218–227. https://doi.org/10.1016/j.cherd.2016.10.030.

Schwertmann, U. 1991 Solubility and dissolution of iron oxides. *Plant and Soil* **130**, 1–25. https://doi.org/10.1007/BF00011851.

Senthil Kumar, P., Ramalingam, S., Abhinaya, R. V., Thiruvengadaravi, K. V., Baskaralingam, P. & Sivanesan, S. 2011 Lead(II) adsorption onto sulphuric acid treated cashew nut shell. *Separation Science and Technology* **46**, 2436–2449. https://doi.org/10.1080/01496395.2011.590174.

Senthilkumar, P., Ramalingam, S., Abhinaya, R. V., Kirupha, S. D., Vidhyadevi, T. & Sivanesan, S. 2012 Adsorption equilibrium, thermodynamics, kinetics, mechanism and process design of zinc(II) ions onto cashew nut shell. *Canadian Journal of Chemical Engineering* **90**, 973–982. https://doi.org/10.1002/cjce.20588.

Soliemanzadeh, A. & Fekri, M. 2017 Synthesis of clay-supported nanoscale zero-valent iron using green tea extract for the removal of phosphorus from aqueous solutions. *Chinese Journal of Chemical Engineering* **25**, 924–930. https://doi.org/10.1016/j.cjche.2016.12.006.

Stefaniuk, M., Oleszczuk, P. & Ok, Y. S. 2016 Review on nano zerovalent iron (nZVI): from synthesis to environmental applications. *Chemical Engineering Journal* **287**, 618–632. https://doi.org/10.1016/j.cej.2015.11.046.

Tarekegn, M. M., Hiruy, A. M. & Dekebo, A. H. 2021 Nano zero valent iron (nZVI) particles for the removal of heavy metals (Cd^{2+}, Cu^{2+} and Pb^{2+}) from aqueous solutions. *RSC Advances* **11**, 18539–18551. https://doi.org/10.1039/D1RA01427G.

Trinh, V. T., Pham, T. T. H., Van, H. T., Trinh, M. V., Thang, P. Q., Vu, X. H., Nguyen, V. Q. & Dang, T. T. 2020 Phosphorus removal from aqueous solution by adsorption using silver nanoparticles: batch experiment. *Journal of Hazardous, Toxic, and Radioactive Waste* **24**, 04020038. https://doi.org/10.1061/(asce)hz.2153-5515.0000529.

Tu, Y. J. & You, C. F. 2014 Phosphorus adsorption onto green synthesized nano-bimetal ferrites: equilibrium, kinetic and thermodynamic investigation. *Chemical Engineering Journal* **251**, 285–292. https://doi.org/10.1016/j.cej.2014.04.036.

Weber, W. 1963 Kinetics of adsorption on carbon from solution. *Journal of the Sanitary Engineering Division* **89**, 31–60.

Wen, Z., Zhang, Y. & Dai, C. 2014 Removal of phosphate from aqueous solution using nanoscale zerovalent iron (nZVI). *Colloids and Surfaces A: Physicochemical and Engineering Aspects* **457**, 433–440. https://doi.org/10.1016/j.colsurfa.2014.06.017.

Wu, D., Shen, Y., Ding, A., Mahmood, Q., Liu, S. & Tu, Q. 2013a Effects of nanoscale zero-valent iron particles on biological nitrogen and phosphorus removal and microorganisms in activated sludge. *Journal of Hazardous Materials* **262**, 649–655. https://doi.org/10.1016/j.jhazmat.2013.09.038.

Wu, D., Shen, Y., Ding, A., Qiu, M., Yang, Q. & Zheng, S. 2013b Phosphate removal from aqueous solutions by nanoscale zero-valent iron. *Environmental Technology* **34**, 2663–2669. https://doi.org/10.1080/09593330.2013.786103.

Yan, L. G., Xu, Y. Y., Yu, H. Q., Xin, X. D., Wei, Q. & Du, B. 2010 Adsorption of phosphate from aqueous solution by hydroxy-aluminum, hydroxy-iron and hydroxy-iron-aluminum pillared bentonites. *Journal of Hazardous Materials* **179**, 244–250. https://doi.org/10.1016/j.jhazmat.2010.02.086.

Yan, J., Han, L., Gao, W., Xue, S. & Chen, M. 2015 Biochar supported nanoscale zerovalent iron composite used as persulfate activator for removing trichloroethylene. *Bioresource Technology* **175**, 269–274. https://doi.org/10.1016/j.biortech.2014.10.103.

Yoon, S. Y., Lee, C. G., Park, J. A., Kim, J. H., Kim, S. B., Lee, S. H. & Choi, J. W. 2014 Kinetic, equilibrium and thermodynamic studies for phosphate adsorption to magnetic iron oxide nanoparticles. *Chemical Engineering Journal* **236**, 341–347. https://doi.org/10.1016/j.cej.2013.09.053.

Yuvakkumar, R., Elango, V., Rajendran, V. & Kannan, N. 2011 1771_Yuvakkaur.pdf 6, pp. 1771–1776.

Zhang, Y., Li, Y., Li, J., Hu, L. & Zheng, X. 2011 Enhanced removal of nitrate by a novel composite: nanoscale zero valent iron supported on pillared clay. *Chemical Engineering Journal* **171**, 526–531. https://doi.org/10.1016/j.cej.2011.04.022.

Zhou, Y., Gao, B., Zimmerman, A. R., Chen, H., Zhang, M. & Cao, X. 2014 Biochar-supported zerovalent iron for removal of various contaminants from aqueous solutions. *Bioresource Technology* **152**, 538–542. https://doi.org/https://doi.org/10.1016/j.biortech.2013.11.021.

Zhu, H., Jia, Y., Wu, X. & Wang, H. 2009 Removal of arsenic from water by supported nano zero-valent iron on activated carbon. *Journal of Hazardous Materials* **172**, 1591–1596. https://doi.org/10.1016/j.jhazmat.2009.08.031.

First received 14 November 2021; accepted in revised form 4 January 2022. Available online 12 January 2022